Supplementary Information

1 Scanning Transmission Electron Microscopy (STEM)

1.1 Thickness of enamel specimens prepared by focused ion beam (FIB)

Section thickness is an important consideration in STEM analysis. For the purposes of this work, sections need to be sufficiently thin and oriented such that a single enamel crystallite spans the entire thickness. For STEM-EELS more generally, it is important to minimize plural scattering, which can obscure core-loss edges and convolve plasmon peaks in the low-loss region.

We therefore established the thickness of section using a literature approach.[1] Briefly, the local thickness of lamellae prepared by FIB, t, can be determined as

$$t = \ln\left(\frac{I_t}{I_0}\right)\lambda \tag{1.1}$$

, where λ is the IMFP, I_t the total number of electrons in the electron energy loss (EEL) spectrum, and I_0 the number of electrons that did not lose energy (*i.e.* the zero-loss peak). The intensities can be determined by integration the EEL spectra for each pixel. The mean free path can be determined as

$$\lambda = \frac{106\ F\ E_0}{E_\mathrm{m}\ \ln(2\beta E_0/E_\mathrm{m})} \tag{1.2}$$

, where E_0 is the energy of the incident beam (in keV), β the collection angle (in mrad), and F a relativistic factor given by

$$F = \frac{1 + (E_0/1022)}{(1 + (E_0/511))^2} \tag{1.3}$$

The average energy loss (in eV), E_m, depends on an effective atomic number Z_eff

$$E_m \approx 7.6{Z_\mathrm{eff}}^{0.36} \tag{1.4}$$

, that is defined as

$$Z_\mathrm{eff} = \frac{\sum_i f_i {Z_i}^{1.3}}{\sum_i f_i {Z_i}^{0.3}} \tag{1.5}$$

, where f_i is the mole fraction of element *I* with atomic number Z_i. Idealizing enamel as stoichiometric OHAp ($Ca_5(PO_4)_3OH$), we estimate λ = 118 nm for these imaging conditions.

Thickness measurements were carried using a GIF Quantum ER system, using a conventional *t*/λ map, integrated in Digital Micrograph 3.2. The beam current was 8.5 pA at 300 kV, with a pixel dwell time of 200 µs. The GIF entrance aperture was 5 mm and the dispersion set to 0.25 eV/channel. The convergence angle was 21.4 mrad, and the collection angle was 40 mrad. For quantitative imaging, we targeted areas in which the section thickness was near 0.2λ, equivalent to 20-30 nm (**Fig. S1**).

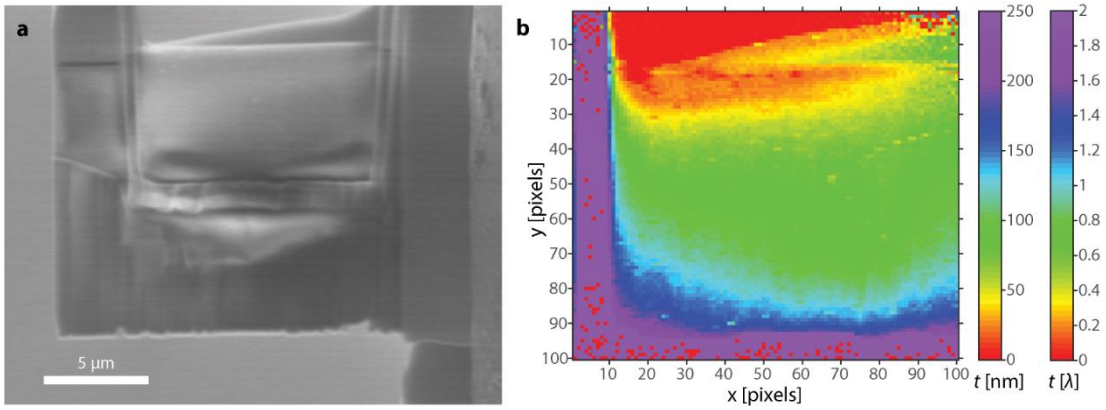

Fig. S1: **Thickness assessment of a FIB-prepared section of human enamel by STEM-EELS. a**. SEM image of a FIB-prepared lamella of human enamel. **b**. EELS thickness map (pixel edge length 180 nm). The left scale indicates the thickness *t* in absolute values, while the scale on right indicates the thickness in units of inelastic mean free path λ.

1.2 Operational parameters for STEM imaging

Table S1. Typical Imaging Conditions for STEM Experiments.

Parameter	Instrument					
	JEM-2100F	GrandARM 300F		Titan Themis		
Acceleration Voltage [kV]	200	300		300		
Aberration-correction	n/a	n/a		Cs		
Imaging Mode	STEM	STEM		STEM		
Nominal Sample Temperature* [˚C]	R.T.	R.T.		< -170˚C		
Convergence semi-angle [mrad]	19.2	29		21.4		
Image contrast	ADF	ADF†	HAADF†	ADF		
Collection semi-angle [mrad]	83.3−183.3	55-106	106-180	39-190		
Probe current [pA]	80	20.8	20.8	4.0	4.0	8.5
Frame edge length [pixels]	2048	2048	2048	2048	4096	1024
Pixel edge length [Å]	3.90	0.64	0.64	0.19	0.09	0.35
Dwell time [µs]	25	2	2	1	1	2
Total dose per exposure [$e^-/Å^2$]	822	635	635	727	2909	873

* The nominal sample temperature was read from a thermocouple near the tip of the sample rod. †ADF and HAADF images collected simultaneously.

1.3 Acquisition and post-processing of cryo-STEM lattice images

Advanced electron optical methods offer seamless integration of structural and chemical information at length scales from hundreds of microns to the atomic scale.[2-4] The obtainable resolution of any experiment, however, is limited by the radiation sensitivity of the material in question. For apatites in general, and for enamel crystallites in particular, the total dose should not surpass 10,000 $e^-/Å^2$.[5-6] This is at least three orders of magnitude lower than what is typically used for atomic-resolution elemental mapping of more robust materials.[7] For analysis of thin sections at atomic resolution, electron radiation artifacts such as radiolysis, mass loss, among others, are strongly reduced by operating at cryogenic conditions.[8] In addition, surface contamination due to carbon migration is minimized.[9] To help mitigate these effects, we therefore performed aberration-corrected scanning transmission electron microscopy at cryogenic temperature (cryo-STEM), using low dose technique (see **Table S1** for typical dose per exposure).

A Gatan 636 dual tilt liquid nitrogen side entry holder was used for cryo-STEM in the Titan Themis. The cryo holder was baked at 100 °C while pumping on the dewar vacuum for 12 hours before use to ensure good thermal insulation of the cryogen during the experiment. Samples were inserted into the microscope at room temperature and the holder was subsequently cooled with liquid nitrogen for at least 2h prior to imaging to allow the temperature to stabilize and thermal drift to subside. Even when fully stabilized, cryo-STEM at the atomic scale often requires fast acquisition to minimize the impact of stage drift. Low-dose imaging further reduces the signal-to-noise ratio of single-frame images. Unless otherwise specified, we therefore used a post-processing approach optimized for these conditions.[4] Specifically, a series of images

of enamel crystallites were collected rapidly (2-4 s/frame), with a total dose of 410-873 $e^{-}/Å^2$ per exposure (e.g. **Fig. S2a**). During post-processing, a number of successive frames were rigidly registered by cross-correlation, and averaged to minimize noise and stage drift (e.g. **Fig. S2b**).[4] This was followed by Fourier-filtering using a Butterworth low pass filter.[10] Specifically, an FFT from an area of the cross-correlated image was computed (e.g. **Fig. S2d**), and multiplied by a 3rd order Butterworth filter with a cutoff frequency of half the sampling frequency (e.g. **Fig. S2e**). Subsequently, the inverse of this filtered FFT was then computed and cropped to the same region of interest as the unfiltered image (**Fig. S2**), to obtain **Figs. 1h** & **1i** in the main text. In some cases, cross-correlation was not necessary, and the image was acquired with a single frame with scan parameters chosen to result in a comparable total dose (**Fig. S3, Fig. 2a**).

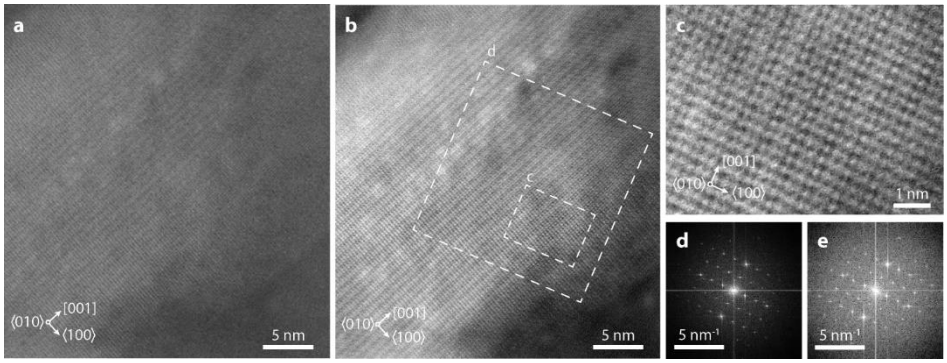

Fig. S2: **Cross-correlation of rapidly acquired high resolution cryo-STEM-ADF images**. **a.** Single frame displaying part of a crystallite oriented to the [010] zone axis. **b.** Cross-correlated and averaged image generated from 9 frames. **c.** Close-up of area indicated in (b) without any additional filtering **d.** FFT computed for the area indicated in (b) (width and height are an integer power of 2). **e.** FFT of (d) multiplied with a Butterworth image of order 3 and a cutoff of half the sampling frequency. The image shown in **Figures 1h&i** are based on the inverse FFT of (e).

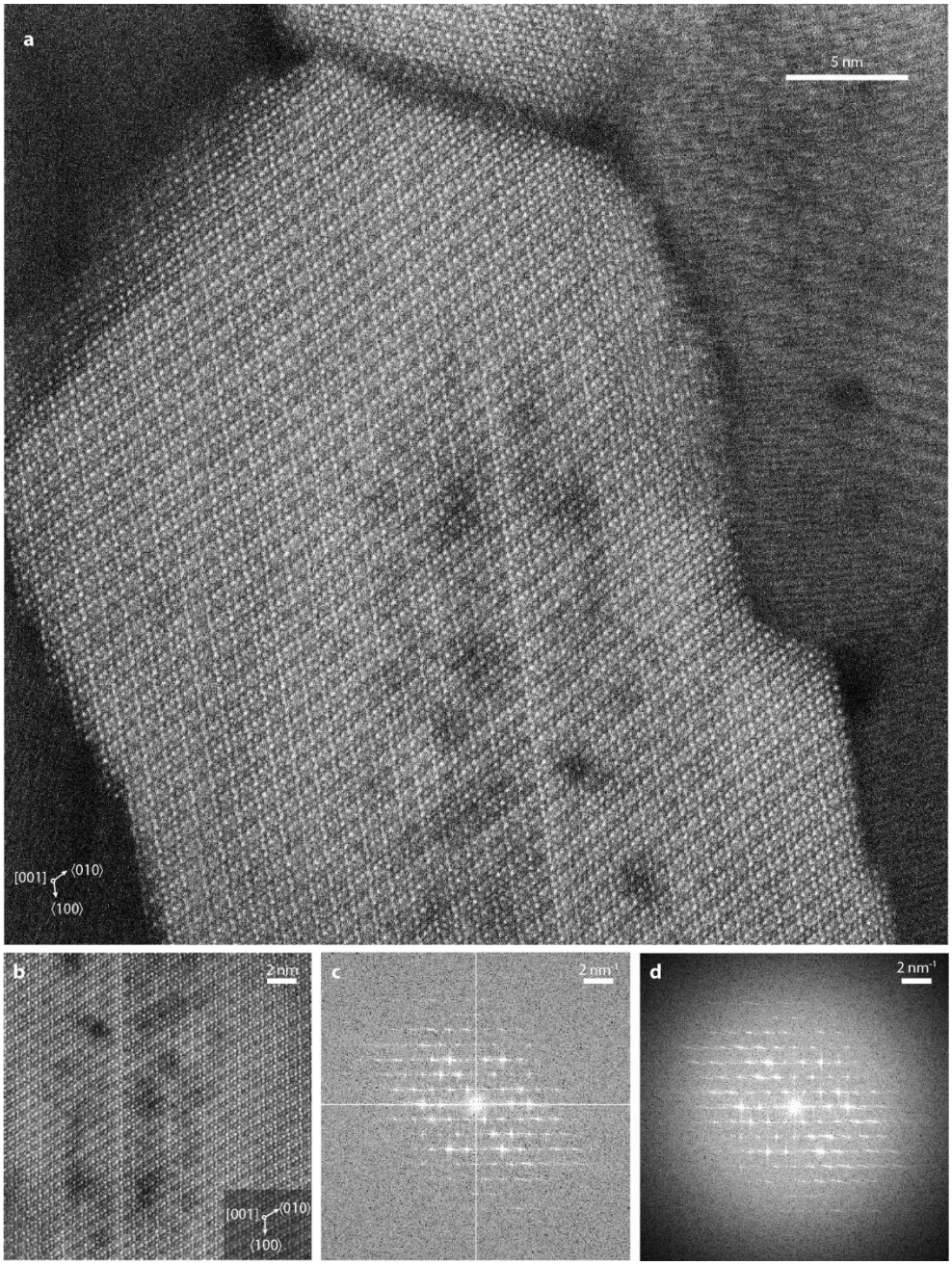

Fig. S3: Atomic scale imaging of enamel crystallites. **a.** Aberration-corrected cryo-STEM-ADF lattice image (unfiltered; single frame) with partial view of several crystallites. The crystallite that appears bright is oriented along the [001] zone axis. **b.** Cropped region of (a) (unfiltered**)**. **c.** FFT of (b). **d.** FFT of (c) multiplied with a 3rd order Butterworth filter with a cutoff frequency of half the sampling frequency. The inverse of this filtered FFT was then computed and cropped to a similar region of interest as the unfiltered image in (b), to obtain **Figure 2a** in the main text.

1.4 Elemental Analysis using STEM-EDS

STEM in conjunction with energy-dispersive X-ray spectroscopy (STEM-EDS) or electron energy loss spectroscopy (STEM-EELS) can enable compositional analysis to the atomic scale. However, quantification – especially of light elements – remains a challenging task.[11] Elemental EDS maps of several enamel crystallites were collected while carefully monitoring the sum spectrum during acquisition. We are confident that beam effects did not affect compositional measurements because relative intensities remained constant while counts increased over the time that the mapping was performed. Furthermore, there were no notable contrast changes in between HAADF images acquired before and after EDS-maps were recorded.

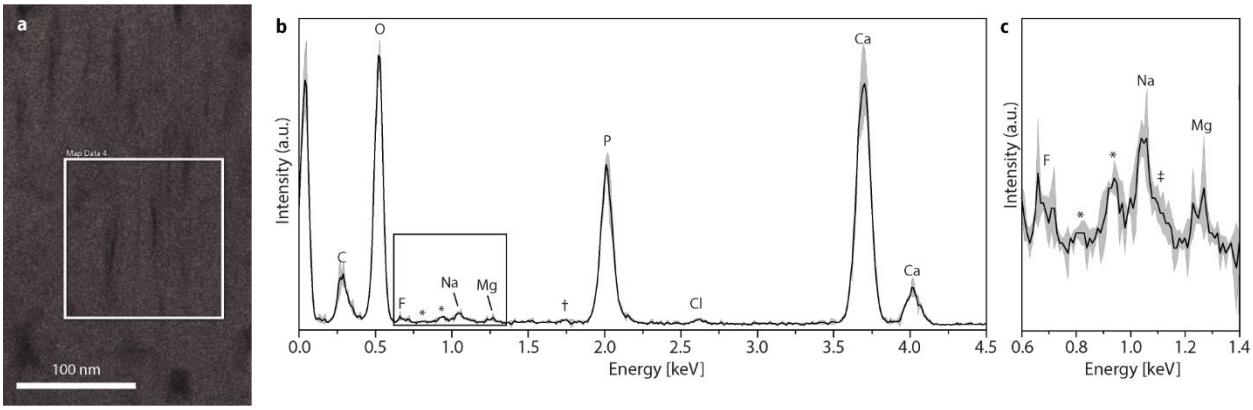

Fig. S4. **STEM-EDS spectrum from nanoscale elemental mappings of fluoridated human enamel**. **a**. STEM-HAADF image of enamel crystallites. **b**. EDS sum spectrum (solid black line) for the total area mapped in (a) (indicated by the white square). Note that a small residual of Si was detected (dagger in (b)), likely from a peak artifact ("escape peak", due to incoming x-rays that have the energy to generate Si x-rays within the silicon drift detector **c**. Close-up of the spectral region indicated in (b). Some Cu was also detected (asterisks), likely a contribution from the TEM grid that was used as a support for the sample. Trace amounts of Ga (double dagger) are likely due to gallium ion implantation during sample preparation by FIB. The shaded area in (b) and (c) represents the error based on the mean ± 3SD, based on N = 3 measurements.

Analysis of the sum spectra revealed that the composition of the crystallites was consistent with the major constituents of typical human tooth enamel in the bulk, and that the variance was small (**Fig. S4** and **Table S2**) . Elemental maps were virtually featureless (not shown) and sum spectra integrated over various regions of interest did not differ from the total sum spectrum. For instance, the magnesium concentration determined from the nanoscale area in **Fig. S4** was ~0.4 at%, the sodium concentration was ~0.7 at%, and the concentration of fluoride ~0.5 at%, i.e. not significantly different from the average values (**Table S2**).

Table S2: Composition of fluoridated human enamel by STEM-EDS

Element	all detected elements		elements expected in enamel	
	X [at%]	σ_X [at%] (N = 3)	X [at%]	σ_X [at%] (N = 3)
C	13.80	2.07	17.57	2.27
O	45.74	0.60	51.96	0.78
F	0.53	0.11	0.47	0.04
Na	0.68	0.10	0.68	0.05
Mg	0.35	0.08	0.37	0.08
P	14.4	0.61	11.68	0.70
Cl	0.31	0.10	0.28	0.01
Ca	21.03	0.80	16.99	0.88
Cu*	2.99	0.13		
Si†	0.11	0.05		
Ga‡	0.06	0.04		
Total	**100**		**100**	

*Likely from TEM grid; †unclear origin; ‡contamination from FIB processing.

1.5 Elemental Analysis using STEM-EELS

We performed elemental mapping on single enamel crystallites using cryo-STEM-EELS in order to explore possible chemical variations within individual crystallites. For typical spectra, please see **Figure 2c-e**. Compared to STEM-EDS, STEM-EELS offered several advantages for this experiment, including higher spatial sensitivity to low concentrations and better energy resolution for chemical analysis of the characteristic edge shapes.[12]

Elemental maps of the Ca $L_{2,3}$, P $L_{2,3}$ and the O *K*-edges indicate that the concentrations of Ca, P and O are often decreased in the intergranular regions with respect to their concentrations in crystallites (**Fig S5**). This observation is consistent with the expectation that the number density of all elements taken together in the intergranular region is lower compared to that of apatite.

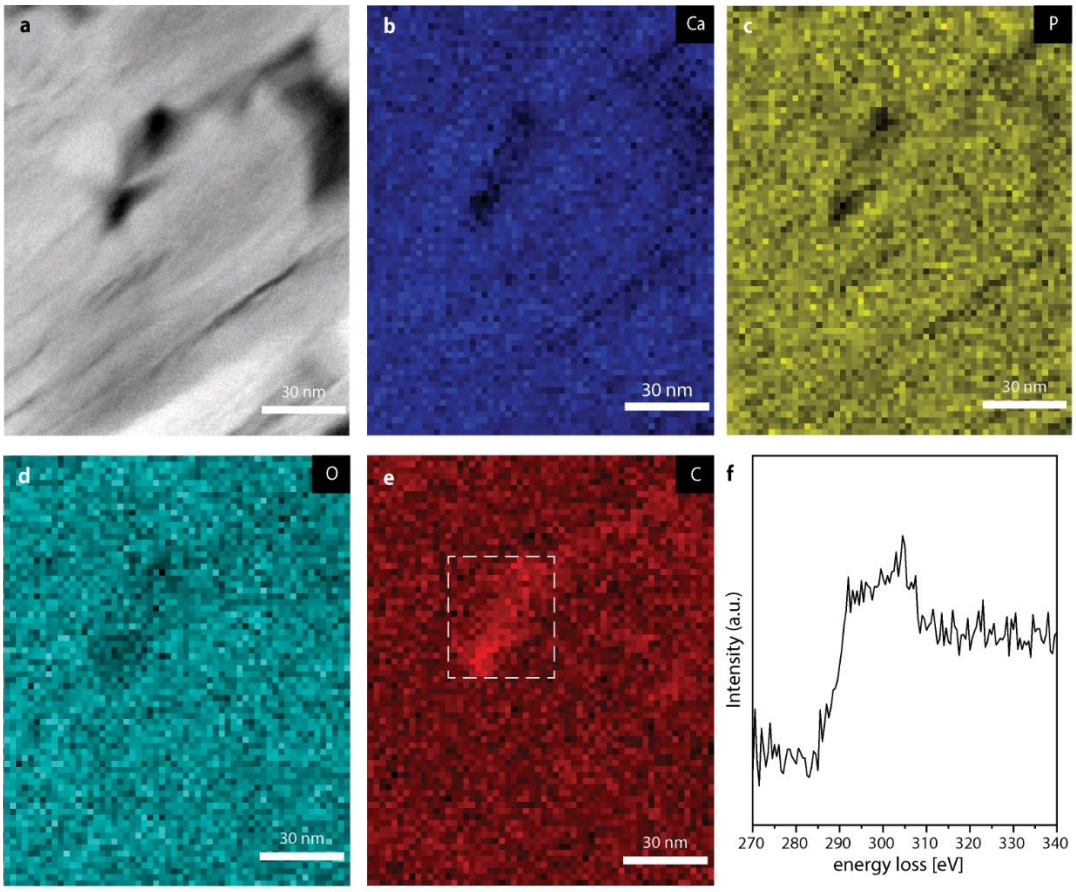

Fig. S5. **Compositional analysis of human enamel crystallites**. **a**. Cryo-STEM-ADF image of several crystallites oriented with their long axis normal to the image plane. Cryo-STEM-EELS spectra shown in **Fig. 2b-f** were integrated over this area. **b-e**. Spectral component maps of Ca $L_{2,3}$-edge (b), P $L_{2,3}$-edge (c), O *K*-edge (d), and Carbon *K*-edge (e). **f**. Background-corrected C *K*-edge cryo-EEL spectrum for the carbon-rich area indicated in (e).

We frequently observed an increase to the C *K*-edge signal in intergranular regions relative to that within crystallites (**Fig S5**). There are indeed indications that small amounts of both inorganic carbon (from carbonates) and organic carbon (from residual proteins) are present in the intergranular phase of enamel.[13-14] In principle, using energy-loss near-edge structure (ELNES) it may be possible to gain insight on the detailed structural and chemical information concerning the oxidation state, molecular bonding and structural organization.[11] For example, careful ELNES analysis may be able to distinguish between residual proteins (sp^2 hybridized) vs. carbonates (sp^3 hybridized). In our EEL spectra, however, the experimental conditions prevent such analysis due to the low spectral signal in our dose-limited conditions.

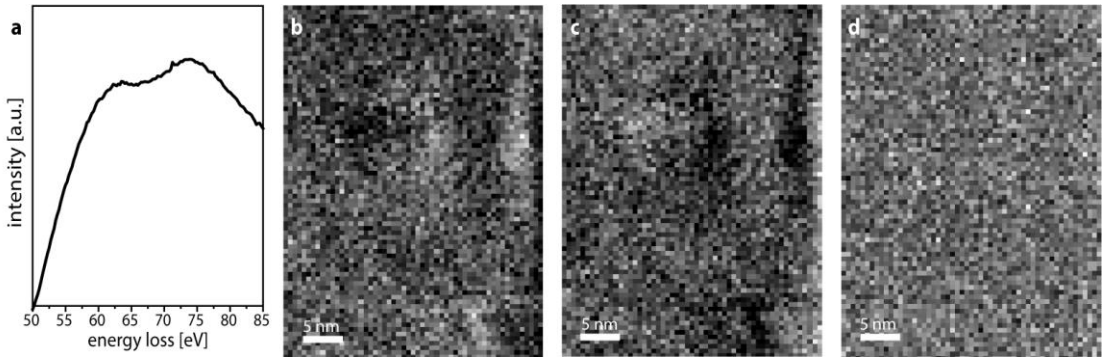

Fig. S6. MCR analysis. a. Close-up of background-corrected cryo-STEM-EEL spectrum near the Mg $L_{2,3}$-edge prior to decomposition into components shown in **Fig. 2f**. **b.** Spatial intensity map for component 2 for area shown in **Fig. 2g**. **c.** Spatial intensity map for component 1 for area shown in **Fig. 2g**. The false-colored composite map shown in **Fig. 2h** is based on (b) and (c). **d.** Plot of the virtually featureless residual.[15] The equation used for this is SC = D, where S is the matrix of spectral components returned by MCR, C is the matrix of concentrations to be solved for and D is the matrix of original data.

2 X-Ray Absorption Spectroscopy

2.1 Results and Discussion

The position and intensity of transitions in Mg *K*-edge X-ray absorption near-edge structure (XANES) spectra are sensitive to the coordination number, geometry, bond length, and order at intermediate range. Many Mg-containing minerals can be identified by their spectral fingerprints.[16] Spectra of rodent enamel lack the *pre-A*, *D*, and *E* features that are characteristic for crystalline dolomite, huntite, and whitlockite (**Fig. S7a**).[13] In contrast, the Mg-rich intergranular phase in rodent incisors shows a striking similarity to spectra of synthetic Mg-substituted amorphous calcium phosphate (Mg-ACP). The dominant feature in spectra of Mg-ACP is the transition associated with the first coordination sphere (feature *B*), with little or no features that depend on order beyond the first shell. At the same time, the lower edge energy is indicative of a lower coordination number and shorter Mg-O bond distance. Spectra of human enamel are similar to those of rodent enamel or synthetic Mg-ACP yet display more pronounced *A* and *B* features. As these features are associated with electronic transitions in the first coordination and multiple scattering events from higher shells, this indicates that a fraction of the Mg in human enamel is present in a crystalline rather than an amorphous environment, consistent with their incorporation into the crystallite core.

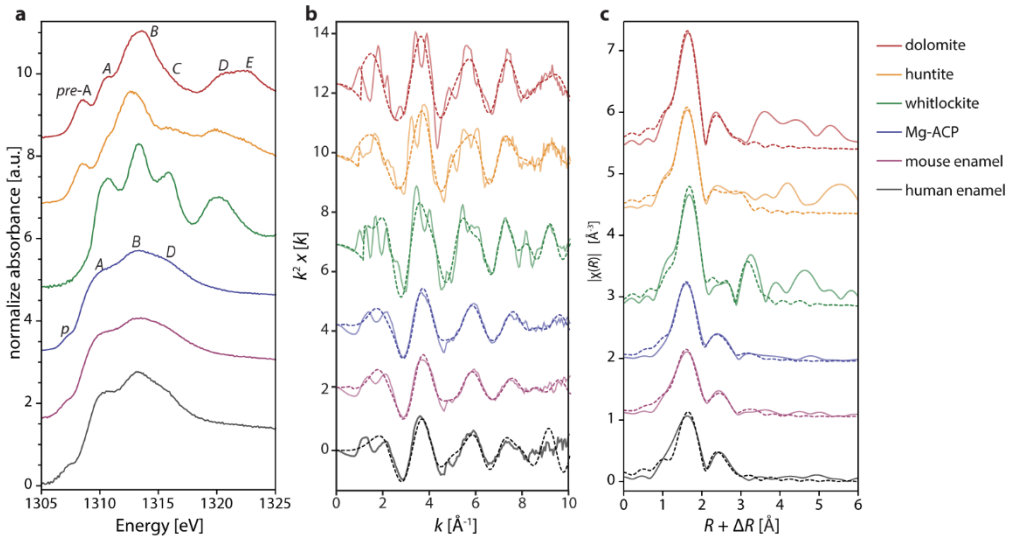

Fig. S7: Comparison of Mg *K*-edge X-ray absorption spectra of dental enamel from different species and reference compounds. Mg ACP, mouse enamel, and reference mineral spectra from [13]. **a**. Mg *K*-edge XANES. **b**. Mg *K*-edge EXAFS (k^2-weighted). **c**. Mg *K*-edge EXAFS (real space).

The Mg *K*-edge extended X-ray absorption fine structure (EXAFS) of human enamel is nearly indistinguishable from that of rodent enamel or synthetic Mg-ACP (**Fig. S7b,c**). In sharp contrast to the crystalline reference compounds, in which numerous scattering features from more distant shells are apparent, spectra of enamel and Mg-ACP are dominated by the nearest neighbor shell. Analysis of the local environment around Mg by fitting EXAFS spectra with theoretical scattering paths (**Table S3**) reveals that the nearest-neighbor Mg-O bond lengths in human enamel (2.09 Å), rodent enamel (2.03 Å) and Mg-ACP (2.02 Å) are notably shorter than Ca-O bonds in OHAp (2.40 Å) and ACP (2.36 Å). Unlike rodent enamel, where the Mg-O bond is shorter than the Mg-O bonds in the crystalline reference compounds (2.08 to 2.11 Å), that of human enamel does fall into the range.[17-18] In human and rodent enamel, and Mg-ACP, this shortening is accompanied by a reduction in the coordination number from 6 to ~4, which is indicative of an amorphous material and/or the presence of water in the first coordination sphere.[16,19] We conclude that the environment of the majority of Mg^{2+} in human enamel exhibits only short- to medium-range order, with a reduction in coordination number, and the possibility of water or hydroxyl ions in the first shell, similar

to the environment of Ca in ACP.[17] However, the Mg-O bond shortening is not as pronounced as in rodent enamel. This is consistent with a fraction of Mg^{2+} occupying disordered Ca[II] sites in the apatite lattice.[20]

Table S3: Mg *K*-edge EXAFS fit parameters.

Sample	Path	R (Å)	CN	σ^2	ΔE (eV)	R-factor
Dolomite	Mg-O_1	2.07(1)	6*	0.0038(9)	4.4	0.7%
	Mg-C	2.99(3)	6*	0.001(3)		
	Mg-O-C	3.14(6)	12*	0.005		
	Mg-O_2	3.48(4)	6*	0.010(8)		
Huntite	Mg-O_1	2.06(1)	6*	0.006(1)	3.5	1.2%
	Mg-C	3.08(8)	6*	0.01(2)		
	Mg-O-C	3.4(2)	12*	0.02		
	Mg-O_2	3.38(4)	6*	0.01(1)		
Whitlockite	Mg-O	2.08(2)	6*	0.006(2)	5.3	5.5%
	Mg-P	3.37(6)	6*	0.006(7)		
	Mg-Ca	3.50(4)	6*	0.004(4)		
Mg-ACP	Mg-O	2.02(2)	3.8(8)	0.005(3)	1.8	1.3%
	Mg-P_1	3.17(6)	3(3)	0.005(9)		
	Mg-P_2	3.39(8)	3(3)	0.005(9)		
Mouse Enamel	Mg-O	2.03(2)	4(1)	0.00899	0.9	1.0%
	Mg-P_1	3.18(6)	3(3)	0.003(9)		
	Mg-P_2	3.40(9)	3(3)	0.003(9)		
Human Enamel	Mg-O	2.09(2)	4†	0.006(3)	-10.9	3.3%
	Mg-P_1	3.08(8)	3†	0.003(8)		
	Mg-P_2	3.28(7)	3†	0.003(8)		

Data for reference compounds was taken from Ref.[13] ΔE was fixed for each individual paths but varied between samples. Bold coordination values were held constant. Uncertainty given in parenthesis for last digit. *designates a CN from crystal structures. †designates CN fixed based on previous work with mouse enamel to improve fit.

3 Atom Probe Tomography

3.1 Introduction

APT dissects a sample atom-by-atom and atomic layer-by-layer, and chemically identifies up to 80% of all atoms in a specimen.[21-22] Unlike methods based on scattering of electrons or X-rays, there is no bias towards elements with high atomic number and the detection limit is typically below 10 atomic ppm. The spatial resolution is in the sub-nanometer range and is independent of the degree of crystallinity. Reconstruction of the identified atoms results in three-dimensional maps of the original sample, which enable sophisticated analyses of compositional gradients, grain boundary segregation, atomic clustering, and other analyses.[23-24] With the recent introduction of UV laser-pulsed APT, the scope of the technique has expanded dramatically and now includes a wide range of poorly conducting samples, including mineralized tissues.[13-14,25-26]

3.2 Principle of Operation

In an atom probe tomograph, a sharpened sample tip (radius ~20-50 nm) is brought into the focal volume of a pulsed UV laser and exposed to a high electric field (15-65 N/nm) generated by a local electrode (**Fig. S8**).[27] The laser pulse, coupled with the electric field, triggers field-evaporation events in which an elemental cation or a small, cationic cluster detach from the surface. Ions are accelerated towards the electrode, and then drift field free until they arrive at a position sensitive detector. The instrument we used, a Cameca LEAP5000XS, has an atomic detection efficiency of ~80%, an improvement by 60% compared to earlier LEAP tomographs. The mass-to-charge-state ratio for each detector event is calculated from the time-of-flight and enables the determination of chemical identity of the ion (**Fig. S9**, **Table S4**). The position of ions in the original sample volume is reconstructed from the sequence and (*x*,*y*) position of detector events.[27-28]

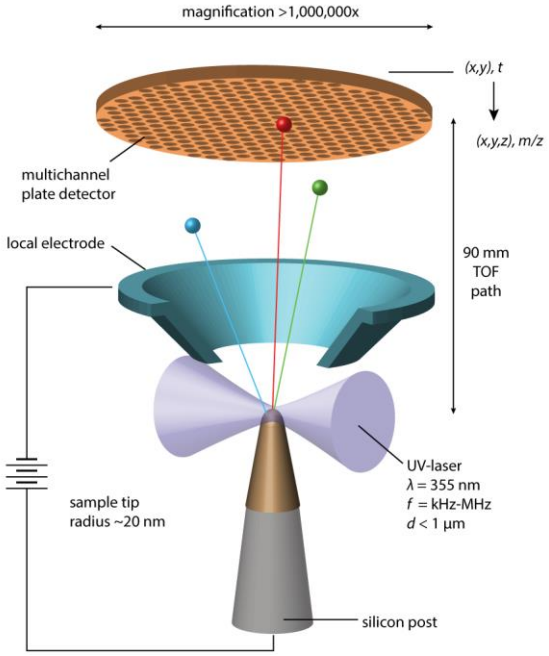

Fig. S8: Schematic drawing of the detection principle of an atom probe tomograph (adapted from [29]).

3.3 Specimens analyzed

A total of 23 samples ('tips') were prepared for analysis by APT. 18 of these represented native samples, and 5 represented samples treated with NaF. During initial quality control, data sets with unsatisfactory

voltage history were excluded. Small data sets (<5-7 M hits) in which the likelihood of finding crystallites with cross sections that are fully included is low were also excluded. Herein, we analyze three APT data sets collected from enamel after treatment with aqueous NaF (yield 60%, **Table S5**, **Fig. S10a-c**), and two data sets that were not treated (yield 11%, **Table S5**, **Fig. S10d,e**).

3.4 APT Mass Spectra and compositional analysis

APT spectra of treated human enamel (**Fig. S9**) closely resemble those of rodent enamel, with ions derived from OHAp as major features (**Table S4**).[13,30] Minor constituents include Mg, Na, F, organic, and inorganic carbon. In addition, trace amounts of Cl^- (<0.1at%), Al (<0.004 at%), and implanted Ga (0.002-0.022 at%) were detected.

Samples that were treated with NaF show a statistically significant increase in the fraction of PO_2F^+ and CaF^+ ions detected (p<0.05, **Table S5**). While the former increases more than five-fold, the latter increases by a factor of more than 22. In fact, CaF^+ makes up about 26% of all fluoride-containing ions in the treated samples, but less than 2% in the untreated ones. The difference is less pronounced for PO_2F^+ (14.3% vs. 4.2%). CaF^+ therefore is an excellent indicator of fluoride introduced to the sample during topical fluoridation. Interestingly, the increase in Na^+ narrowly misses the p<0.05 significance level, however, the magnitude of its change appears about 2-fold greater than that of the fluoride-containing ions. A few other ions are also affected, but the difference in their concentrations is 1-2 orders of magnitude less than for the fluoride-containing ions and Na^+. The only exception is Cl^-, of which about 0.8at% is lost on treatment with NaF, likely as part of an ion-exchange mechanism.

While the effect of NaF treatment on the fraction of PO_2F^+ and CaF^+ detected is significant, several other ions contribute to the overall fluorine content (**Table S5**). The most important ones are POF^+ (42% of all fluoride-containing ions in treated samples vs. 66% in untreated samples) and F^+ (8% vs. 11%), neither of which shows a significant change between treated and untreated samples. This is probably the reason why, after decomposition into atoms, the difference in the fluorine content of treated and untreated samples is no longer significant (**Table S6**). In fact, of the minority elements Mg, Na, F, and C, only Na^+ shows significant difference, and then only at the p<0.1 level.

Taken together, we conclude that there is an increase in fluoride and sodium content with NaF treatment. However, comparison of a larger number of data sets will be required to increase confidence in absolute numbers (F: +0.21at%, +58% relative increase; Na: +0.39at%, +71% relative increase). More importantly, we expect that CaF^+ ions in the reconstructions of treated samples will reveal regions in enamel that are accessible to topically supplied fluoride.

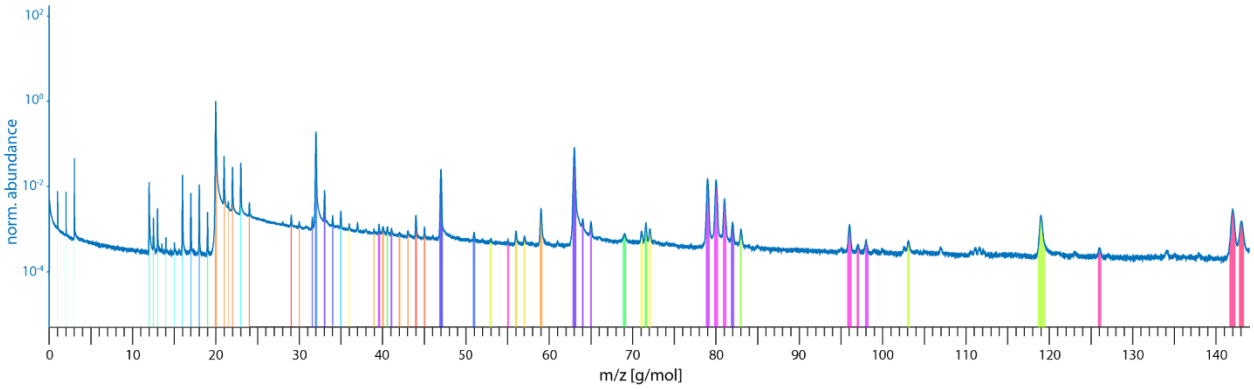

Fig. S9: Representative ranged mass spectrum of fluoridated human enamel.

Table S4. Ions identified in representative APT spectrum of enamel.

Formula	Charge State	m/z (calc'd) [Da]	m/z (expt) [Da]	integration lower limit [Da]	integration upper limit [Da]	integral
^{1}H	+	1.01	1.01	1.00	1.02	108.01
$^{1}H_2$	+	2.01	2.02	2.00	2.02	118.99
$^{1}H_3$	+	3.02	3.02	3.00	3.03	597.32
^{24}Mg	2+	11.99	12.00	11.95	12.06	631.58
^{25}Mg	2+	12.49	12.50	12.45	12.55	98.19
^{26}Mg	2+	12.99	13.00	12.97	13.04	137.67
^{27}Al	2+	13.50	13.51	13.47	13.53	23.05
$^{12}C^{1}H_2$	+	14.00	14.01	13.98	14.03	27.68
$^{12}C^{1}H_3$	+	15.01	15.03	14.99	15.06	27.30
^{16}O	+	15.99	16.00	15.94	16.05	856.86
$^{16}O^{1}H$	+	17.00	17.01	16.95	17.07	365.15
$^{16}O^{1}H_2$	+	18.00	18.01	17.95	18.07	566.05
^{19}F	+	19.00	19.01	18.96	19.06	138.43
^{40}Ca	2+	19.98	19.99	19.88	20.11	65061.59
^{42}Ca	2+	20.98	21.00	20.94	21.06	3275.86
^{43}Ca	2+	21.48	21.50	21.46	21.53	283.41
^{44}Ca	2+	21.98	22.00	21.95	22.06	1922.22
^{23}Na	+	22.99	22.99	22.92	23.06	2590.61
^{48}Ca	2+	23.98	24.01	23.96	24.07	346.51
$^{12}C^{16}O$	+	28.00	28.03	27.96	28.07	148.70
$^{12}C^{16}O^{1}H$	+	29.00	29.03	28.97	29.10	221.07
$^{12}C^{16}O_3$	2+	29.99	30.02	29.95	30.06	145.48
$^{31}P^{16}O_2$	2+	31.50	31.56	31.50	31.63	203.38
$^{16}O_2$	+	31.99	32.00	31.87	32.14	17962.49
$^{31}P^{16}O^{19}F$	2+	32.98	33.03	32.95	33.12	825.72
$^{1}H_2{}^{16}O_2$	+	34.01	34.01	33.93	34.08	244.92
^{35}Cl	+	35.00	35.00	34.91	35.08	321.77
$^{40}Ca^{16}O_2$	2+	35.98	35.99	35.95	36.06	130.77
^{37}Cl	+	37.00	36.99	36.91	37.08	198.06
$^{40}Ca^{16}O_2$	2+	38.00	38.03	37.93	38.11	157.13
$^{40}Ca^{19}F_2$	2+	38.98	38.94	38.89	39.05	139.07
$^{31}P^{16}O_3$	2+	39.48	39.57	39.44	39.71	261.90
^{40}Ca	+	39.96	40.05	39.95	40.15	200.09
$^{31}P^{16}O_2{}^{19}F$	2+	40.98	41.10	40.97	41.17	180.17
^{42}Ca	+	41.96	42.02	41.93	42.12	141.60
^{43}Ca	+	42.96	43.06	42.96	43.12	126.97
$^{12}C^{16}O_2$	+	43.99	44.01	43.91	44.12	306.48
$^{12}C^{16}O_2{}^{1}H$	+	45.00	45.03	44.95	45.12	145.07
$^{31}P^{16}O$	+	48.97	47.00	46.82	47.23	3492.76
$^{16}O_2{}^{19}F$	+	50.99	51.01	50.83	51.11	182.28
$^{20}Ca^{31}P^{16}O^{19}F$	2+	52.96	52.98	52.85	53.07	118.59
$^{31}P_2{}^{16}O_3$	2+	54.97	55.05	54.95	55.15	96.93
$^{40}Ca^{16}O$	+	55.96	56.00	55.90	56.12	156.21
$^{40}Ca^{16}O^{1}H$	+	56.97	57.06	56.91	57.11	117.92
$^{40}Ca^{19}F$	+	58.96	59.00	58.86	59.18	581.11
$^{31}P^{16}O_2$	+	62.96	63.00	62.79	63.24	14432.94
$^{31}P^{16}O_2{}^{1}H$	+	63.97	64.02	63.91	64.11	292.00
$^{31}P^{16}O_2{}^{1}H_2$	+	64.98	65.00	64.90	65.10	248.61
^{69}Ga	+	68.93	69.03	68.83	69.23	265.84
$^{40}Ca^{31}P$	+	70.94	71.09	70.95	71.20	181.78
$^{40}Ca_2{}^{31}P^{16}O_2$	2+	71.44	71.60	71.44	71.73	295.03
$^{40}Ca^{16}O_2$	+	71.95	72.11	71.96	72.20	205.27
$^{31}P^{16}O_3$	+	78.96	79.00	78.78	79.24	3321.49
$^{31}P^{16}O_3{}^{1}H$	+	79.97	80.03	79.78	80.24	3243.06
$^{31}P^{16}O_3{}^{1}H_2$	+	80.97	81.03	80.83	81.25	1182.78
$^{31}P^{16}O_2{}^{19}F$	+	81.96	81.99	81.80	82.18	374.21
$^{40}Ca^{31}P_2{}^{16}O_4$	2+	82.94	82.98	82.86	83.11	199.15
$^{31}P^{16}O_4{}^{1}H$	+	95.96	96.04	95.74	96.29	402.34
$^{31}P_2{}^{16}O^{19}F$	+	96.94	97.05	96.89	97.16	101.10
$^{31}P^{16}O_3{}^{19}F$	+	97.96	98.03	97.89	98.30	167.81
$^{40}Ca^{31}P^{16}O_2$	+	102.93	103.09	102.94	103.24	134.20
$^{40}Ca^{31}P^{16}O_3$	+	118.92	118.97	118.62	119.54	879.29
$^{31}P_2{}^{16}O_4$	+	125.93	126.00	125.84	126.23	120.21
$^{31}P_2{}^{16}O_5$	+	141.92	142.02	141.60	142.35	1169.66
$^{31}P_2{}^{16}O_5{}^{1}H$	+	142.93	143.06	142.75	143.36	650.81
$^{31}P_3{}^{16}O_4{}^{1}H$	+	157.91	157.99	157.65	158.38	328.09
$^{31}P_3{}^{16}O_4{}^{1}H_2$	+	158.92	158.99	158.76	159.30	196.50
$^{40}Ca_2{}^{16}O_5$	+	159.90	160.06	159.79	160.34	208.25
$^{40}Ca_2{}^{16}O_5{}^{1}H$	+	160.91	161.02	160.74	161.23	138.63
$^{40}Ca_2{}^{31}P_3{}^{16}O_2$	+	204.84	205.17	204.15	206.13	430.09

Table S5. Comparison of Ion Fraction in NaF-treated and untreated samples. X_i^T indicates the fraction of all ions for a given ionic species in the *i*-th treated sample, X_j^U indicates the fraction in the *j*-th untreated sample.

species	NaF treated			untreated					
	X_1^T	X_2^T	X_3^T	X_1^U	X_2^U	$\bar{X}^T$	$\bar{X}^U$	$\bar{X}^T - \bar{X}^U$	p*
Al	4.76E-05	7.42E-05	5.64E-05	0.00E+00	0.00E+00	5.94E-05	0.00E+00	5.94E-05	0.01†
Cl	1.58E-03	1.57E-03	1.26E-03	2.25E-03	2.36E-03	1.47E-03	2.31E-03	-8.35E-04	0.01†
H_2	8.90E-04	1.33E-03	1.11E-03	2.31E-04	8.85E-05	1.11E-03	1.60E-04	9.50E-04	0.01†
PO_2F§	1.70E-03	1.51E-03	1.16E-03	9.67E-05	4.52E-04	1.46E-03	2.74E-04	1.18E-03	0.02†
CH_2	1.03E-04	1.67E-04	1.82E-04	3.80E-06	0.00E+00	1.51E-04	1.90E-06	1.49E-04	0.02†
CH_3	7.86E-05	8.39E-05	7.98E-05	3.60E-05	0.00E+00	8.08E-05	1.80E-05	6.28E-05	0.02†
P_2O_4	2.14E-04	2.28E-04	1.16E-04	3.68E-04	3.64E-04	1.86E-04	3.66E-04	-1.80E-04	0.03†
CaF§	3.44E-03	1.65E-03	2.85E-03	0.00E+00	2.33E-04	2.65E-03	1.17E-04	2.53E-03	0.03†
CaP_2O_4	6.89E-04	6.05E-04	3.38E-04	0.00E+00	9.11E-05	5.44E-04	4.56E-05	4.99E-04	0.04†
H_3	4.75E-03	9.34E-03	6.96E-03	1.90E-03	1.49E-03	7.02E-03	1.70E-03	5.32E-03	0.05‡
Na§	1.85E-02	1.40E-02	1.73E-02	7.52E-03	1.18E-02	1.66E-02	9.67E-03	6.92E-03	0.06‡
PO_2H_2	7.49E-04	1.04E-03	5.51E-04	5.42E-05	4.00E-04	7.78E-04	2.27E-04	5.51E-04	0.09‡
O_2F	2.87E-04	3.20E-04	1.94E-04	3.63E-04	4.83E-04	2.67E-04	4.23E-04	-1.56E-04	0.10
H	7.59E-04	6.55E-04	5.91E-04	3.07E-04	5.36E-04	6.68E-04	4.21E-04	2.47E-04	0.10
Mg	6.42E-03	5.15E-03	6.69E-03	4.92E-03	4.42E-03	6.09E-03	4.67E-03	1.42E-03	0.11
$CaPO_2$	3.04E-04	3.49E-04	1.29E-04	5.66E-04	3.72E-04	2.61E-04	4.69E-04	-2.08E-04	0.16
CO_2H	3.74E-04	3.12E-04	1.90E-04	6.88E-05	2.29E-04	2.92E-04	1.49E-04	1.43E-04	0.22
O_2	1.44E-01	1.48E-01	1.53E-01	1.96E-01	1.51E-01	1.48E-01	1.73E-01	-2.48E-02	0.24
PO_2H	5.12E-04	6.06E-04	1.24E-04	4.99E-04	8.87E-04	4.14E-04	6.93E-04	-2.79E-04	0.33
CO_2	1.34E-03	1.40E-03	1.03E-03	4.51E-04	1.29E-03	1.26E-03	8.72E-04	3.87E-04	0.35
$CaPO_3$	5.27E-03	6.01E-03	5.08E-03	4.27E-03	5.41E-03	5.45E-03	4.84E-03	6.18E-04	0.35
PO_2	1.15E-01	1.24E-01	1.14E-01	9.55E-02	1.19E-01	1.18E-01	1.07E-01	1.04E-02	0.36
CaP	5.07E-04	4.21E-04	3.03E-04	2.74E-04	3.73E-04	4.10E-04	3.23E-04	8.71E-05	0.38
CaO	4.59E-04	4.11E-04	2.84E-04	1.25E-04	4.16E-04	3.85E-04	2.71E-04	1.14E-04	0.44
P	0.00E+00	4.79E-04	0.00E+00	0.00E+00	0.00E+00	1.60E-04	0.00E+00	1.60E-04	0.50
CO	1.05E-04	2.47E-04	7.16E-05	1.43E-05	1.49E-04	1.41E-04	8.15E-05	5.96E-05	0.54
Ca_2O_5	6.24E-04	8.22E-04	2.09E-04	2.70E-04	1.52E-03	5.52E-04	8.95E-04	-3.43E-04	0.56
PO_3	2.50E-02	2.27E-02	2.04E-02	2.35E-02	2.42E-02	2.27E-02	2.38E-02	-1.11E-03	0.57
PO	2.64E-02	2.75E-02	2.71E-02	2.93E-02	2.60E-02	2.70E-02	2.76E-02	-6.50E-04	0.65
F	9.09E-04	7.89E-04	8.11E-04	3.77E-04	1.07E-03	8.36E-04	7.21E-04	1.15E-04	0.69
Ca	5.69E-01	5.47E-01	5.82E-01	5.92E-01	5.56E-01	5.66E-01	5.74E-01	-8.04E-03	0.70
CaOH	2.42E-04	1.74E-04	9.95E-05	2.35E-05	2.39E-04	1.72E-04	1.31E-04	4.07E-05	0.70
P_3O_4H	1.29E-03	1.52E-03	9.89E-04	7.35E-04	1.51E-03	1.27E-03	1.12E-03	1.46E-04	0.71
PO_3H_2	7.26E-03	8.38E-03	4.44E-03	3.37E-04	1.03E-02	6.69E-03	5.34E-03	1.36E-03	0.76
PO_3H	2.35E-02	2.90E-02	1.81E-02	1.01E-02	3.13E-02	2.35E-02	2.07E-02	2.82E-03	0.77
O_2H_2	5.69E-04	5.58E-04	4.02E-04	2.42E-04	6.69E-04	5.10E-04	4.55E-04	5.46E-05	0.77
OH_2	4.35E-03	4.59E-03	3.72E-03	2.37E-03	5.45E-03	4.22E-03	3.91E-03	3.07E-04	0.81
P_2O_3	7.09E-05	6.38E-05	5.92E-05	4.90E-05	7.50E-05	6.46E-05	6.20E-05	2.65E-06	0.82
P_2O_5	7.79E-03	8.83E-03	6.69E-03	7.33E-03	8.67E-03	7.77E-03	8.00E-03	-2.29E-04	0.82
Ca_2PO_2	1.20E-03	1.34E-03	6.22E-04	1.30E-04	1.68E-03	1.06E-03	9.04E-04	1.51E-04	0.83
Ga	3.98E-04	4.14E-05	6.12E-05	0.00E+00	4.32E-04	1.67E-04	2.16E-04	-4.88E-05	0.84
O	6.76E-03	8.46E-03	8.47E-03	9.15E-03	6.07E-03	7.90E-03	7.61E-03	2.88E-04	0.85
PO_3F	2.59E-04	3.33E-04	1.48E-04	6.93E-05	3.73E-04	2.47E-04	2.21E-04	2.53E-05	0.86
P_2O_5H	2.92E-03	3.40E-03	1.18E-03	4.98E-04	5.24E-03	2.50E-03	2.87E-03	-3.71E-04	0.86
CaO2	8.95E-04	1.13E-03	4.09E-04	1.96E-04	1.28E-03	8.12E-04	7.38E-04	7.36E-05	0.89
$P_3O_4H_2$	6.09E-04	6.09E-04	1.75E-04	1.46E-04	8.73E-04	4.64E-04	5.09E-04	-4.49E-05	0.90
OH	2.71E-03	2.81E-03	2.39E-03	2.05E-03	3.14E-03	2.64E-03	2.59E-03	4.56E-05	0.92
CaPOF	8.91E-05	1.32E-04	6.92E-05	4.23E-05	1.60E-04	9.68E-05	1.01E-04	-4.29E-06	0.94
P_2OF	1.71E-04	1.53E-04	5.51E-05	5.44E-05	2.11E-04	1.26E-04	1.33E-04	-6.30E-06	0.94
Ca_2O_5H	3.07E-04	3.50E-04	7.01E-05	1.15E-04	3.92E-04	2.42E-04	2.53E-04	-1.10E-05	0.95
PO_4H	1.93E-03	1.91E-03	1.26E-03	9.72E-04	2.37E-03	1.70E-03	1.67E-03	2.84E-05	0.96
COH	5.94E-04	4.47E-04	4.85E-04	2.65E-04	7.69E-04	5.09E-04	5.17E-04	-8.17E-06	0.97
POF	4.63E-03	4.40E-03	3.79E-03	2.39E-03	6.24E-03	4.27E-03	4.32E-03	-4.52E-05	0.98
$Ca_2P_3O_2$	1.34E-03	1.48E-03	1.50E-03	1.65E-03	1.23E-03	1.44E-03	1.44E-03	-3.19E-06	0.99
CO_3	2.36E-04	2.55E-04	1.18E-04	5.80E-05	3.51E-04	2.03E-04	2.05E-04	-1.85E-06	0.99
CaF_2	1.80E-04	1.06E-04	7.05E-05	6.67E-05	1.70E-04	1.19E-04	1.18E-04	5.92E-07	0.99
sum	**1**	**1**	**1**	**1**	**1**	**1**	**-**	**-**	**-**

***** The *p*-value determined by 1-way analysis of variance (ANOVA) is the probability that the difference of the means $\bar{X}^T - \bar{X}^U$ is observed if the null hypothesis that there is no difference in means is true. The null hypothesis is rejected if $p < \alpha$, where α is the significance level. †*p*-Values smaller than α = 0.05.‡p-Values between 0.05 and 0.1. §Rows corresponding to ions singled out in the discussion.

Table S6: Bulk composition of enamel according to APT analyses.

Sample	human premolar, fluoridated					human premolar, native				1-way ANOVA
	1	2	3	$\bar{X}$	$\frac{\sigma}{\bar{X}}$ [%]†	1	2	$\bar{X}$	$\frac{\sigma}{\bar{X}}$ [%]	p‡
#detector events [10^6]	27.8	28	60			35	9.1			
#ranged atoms [10^6]	21.9	15.4	40.4			16.9	6.07			
X_{Cl} [at%]	0.09	0.08	0.07	0.08	9	0.14	0.13	0.13	06	0.01§
¶X_{Na} [at%]	1.03	0.75	1.01	0.93	17	0.46	0.63	0.54	22	0.06‖
X_O [at%]	46.91	48.17	46.11	47.06	2	48.79	48.94	48.87	0.2	0.10
X_F [at%]	0.66	0.52	0.55	0.58	13	0.22	0.51	0.36	56	0.18
X_{Mg} [at%]	0.36	0.28	0.39	0.34	17	0.30	0.23	0.27	17	0.24
X_C [at%]	0.16	0.16	0.13	0.15	12	0.05	0.15	0.10	65	0.31
X_H [at%]	4.37	5.49	3.95	4.60	17	1.72	4.60	3.16	65	0.32
X_{Ga} [at%]	0.02	0.00	0.00	0.01	120	0	0.02	0.02		0.40
X_P [at%]	13.75	14.32	12.96	13.67	5	11.70	14.31	13.01	14	0.58
X_{Ca} [at%]	32.66	30.23	34.84	32.58	7	36.62	30.48	33.55	13	0.76

†Relative uncertainty calculated as the ratio of the standard deviation over the mean. ‡The *p*-value determined by 1-way analysis of variance (ANOVA) is the probability that the difference of the mean of mole fractions of the fluoridated and the native sample is observed if the null hypothesis (that there is no difference in means) is true. The null hypothesis is rejected if $p < \alpha$, where α is the significance level. §*p*-Values smaller than α = 0.05. ‖p-values between 0.05 and 0.1. ¶Rows corresponding to elements singled out in the discussion.

3.5 Overview of reconstructed data sets.

In reconstructions of NaF-treated samples, CaF^+ ions clearly outline individual crystallites. In untreated samples, on the other hand, hardly any CaF^+ ions are detected (**Table S5, Figure S10**). This strongly suggests that CaF^+ is an indicator for the amorphous intergranular phase, and that fluoride ions diffuse much more rapidly in the intergranular phase than in the crystallites themselves.

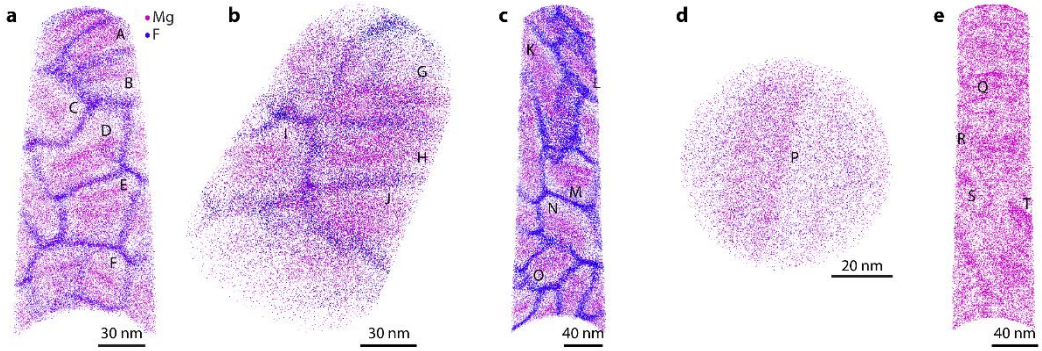

Fig. S10: **3D-reconstructions of treated (a-c) and un-treated (d,e) human enamel**, oriented such that the view direction is approximately parallel to the long axis of the crystallites. For tips **a-d**, Mg ions (*m*/z = 12, 12.5, 13 Da) and CaF ions (*m*/z = 59 Da) are rendered. There was no CaF present in the mass spectrum for tip **e**, so only Mg ions are rendered. 1D concentration profiles were taken across each numbered crystallite and plotted in **Fig S13**.

3.6 Reconstruction of an untreated sample.

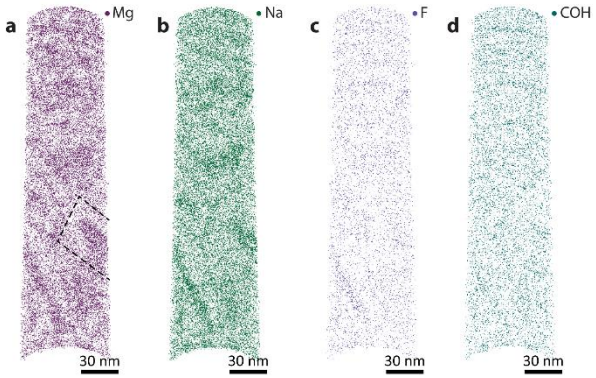

Fig. S11: APT reconstruction of un-treated human enamel, oriented such that the view direction is approximately parallel to the long axis of the crystallites. **a**. Rendering of Mg ions (m/z = 12, 12.5, 13 Da), **b**. Rendering of Na ions (m/z = 23). **c**. Rendering of F ions (m/z = 19). **d**. Rendering of COH ions (m/z = 29). The boundaries of one crystallite are indicated in (a).

3.7 3D rendering of reconstruction of a single crystallite

To better convey both the three-dimensionality of the data, we include two movies. Both represent a 30 nm thick slice through the same enamel crystallite (crystallite D in **Fig S10**, profile (d) in **Fig. S12**, from an enamel sample treated with aqueous NaF), equivalent to the thickness of a section for STEM. The slice was rotated such that the view axis (*x*-axis) is approximately parallel to the Mg layers. Reconstructions are rotated about the *z*-axis (**Video S1**), and about the *z*- and *y*-axes (**Video S2**). The spatial distribution of all detected $^{24}Mg^{2+}$, $^{40}Ca^{19}F^+$, $^{23}Na^+$, and $CO_xH_y^+$-ions in space, i.e. the point cloud nature of the data is highlighted in **Video S1**. A rendering of iso-(concentration) surfaces for $^{24}Mg^{2+}$ (0.1 ions/nm^3), $^{23}Na^+$ (0.3 ions/nm^3), and $CO_xH_y^+$-ions (0.12 ions/nm^3) framed by an isosurface for $^{40}Ca^{19}F^+$(0.1 ions/nm^3), as the latter neatly defines the intergranular phase. Iso-concentration surfaces are the 3D equivalent of contourlines.

We note that the Mg layers appear a little irregular rather than strictly plate-like. The isosurfaces for Na^+, and $CO_xH_y^+$-ions, and to a lesser degree that for CaF^+ similarly indicate local fluctuations rather than

smooth gradients. It is currently not clear whether this is because of statistical fluctuations (Poisson noise), or because there is some sort of ion clustering. The "patchy" contrast observed in STEM could be seen as a support of the latter. However, a correlative analysis similar to that required for linking the layered structure to the central dark line feature would be required to make a firm statement one way or another

3.8 Extraction of 1D concentration profiles.

Identifying the core-shell structure and Mg layers in crystallites is generally straightforward by rotating the 3D reconstruction on a computer screen. In any given rendering, however, the slight misorientation of crystallites against each other is frequently sufficient to obscure layers in all but one crystallite. Capturing representative concentration profiles for individual crystallites is more demanding. Given relatively low concentration of the relevant ions and the very intricate structure, we found that powerful tools such as proxigrams and cluster analysis are not immediately helpful. This is primarily due to the difficulty of defining smooth concentration isosurfaces for the former, and problems of differentiating between atoms in different environments, such as the amorphous intergranular phase and the crystallite core.

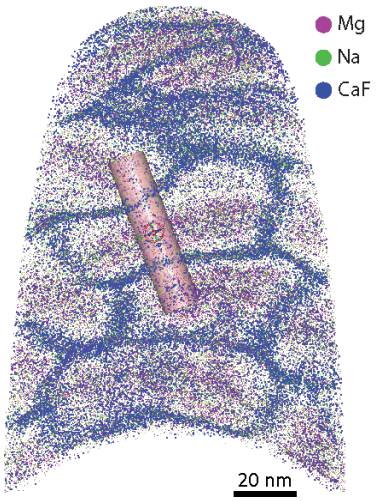

Fig. S12: APT reconstruction of fluoridated human enamel. Rendering showing positions of Mg ions (magenta), Na ions (green) and CaF+ (blue). Line profiles given in Fig. 3d were using IVAS® in the cylindrical volume indicated. Mole fractions were averaged within a disk (d = 12.5 nm, h = 51 nm), which was then swept along the long axis of the cylinder.

We therefore used 1D concentration profiles that were integrated along paths defined manually in IVAS® (**Fig. S12**). We note that features are rarely perfectly planar, and profiles only approximately normal to the plane. Profiles depicted in **Fig. S13** for the 20 crystallites indicated in **Fig. S10** are therefore likely somewhat broadened compared to the actual distribution. To the best of our knowledge, there is currently no accepted way to determine statistical significance for the comparison of peak amplitudes or integrals for individual line profiles that report mole fraction. One of the issues is that mole fractions are correlated with each other; this makes it rather complex to propagate uncertainty based on counting statistics. To address this to the best of our ability, we report means and ranges taken across the set of line profiles in the main manuscript and also show the data in **Fig. S13** to provide a feel for the signal to noise ratio.

Inspection of these profiles that

- The mole fraction of Mg, representing Mg^{2+}, and of C, representing CO_3^{2-}, are elevated in the intergranular phase in both untreated and NaF-treated samples.
- The mole fractions of Na^+ and F^- are additionally elevated in the intergranular phase of fluoridated samples.
- While the distributions in the intergranular phase largely overlap, maxima do not always occur at the exact same position.
- In all 20 profiles, there is a core that is elevated in Na (Na^+), Mg (Mg^{2+}), F (F^-), and C (CO_3^{2-}), surrounded by a shell that is depleted, but not devoid, of these constituents. The distributions of Na^+, F^-, and CO_3^{2-} are broad, not necessarily symmetric, and at time have shoulders or appear bi- or even multimodal. Where several maxima are present, they are usually closely spaced.
- The Mg^{2+} distribution differs from those of the other minor constituents in that it is always bimodal, and the peaks are spaced more widely, essentially flanking the core. The two maxima in the Mg distribution are not necessarily of equal height.

3.9 1D concentration profiles for crystallites identified in Fig. S10

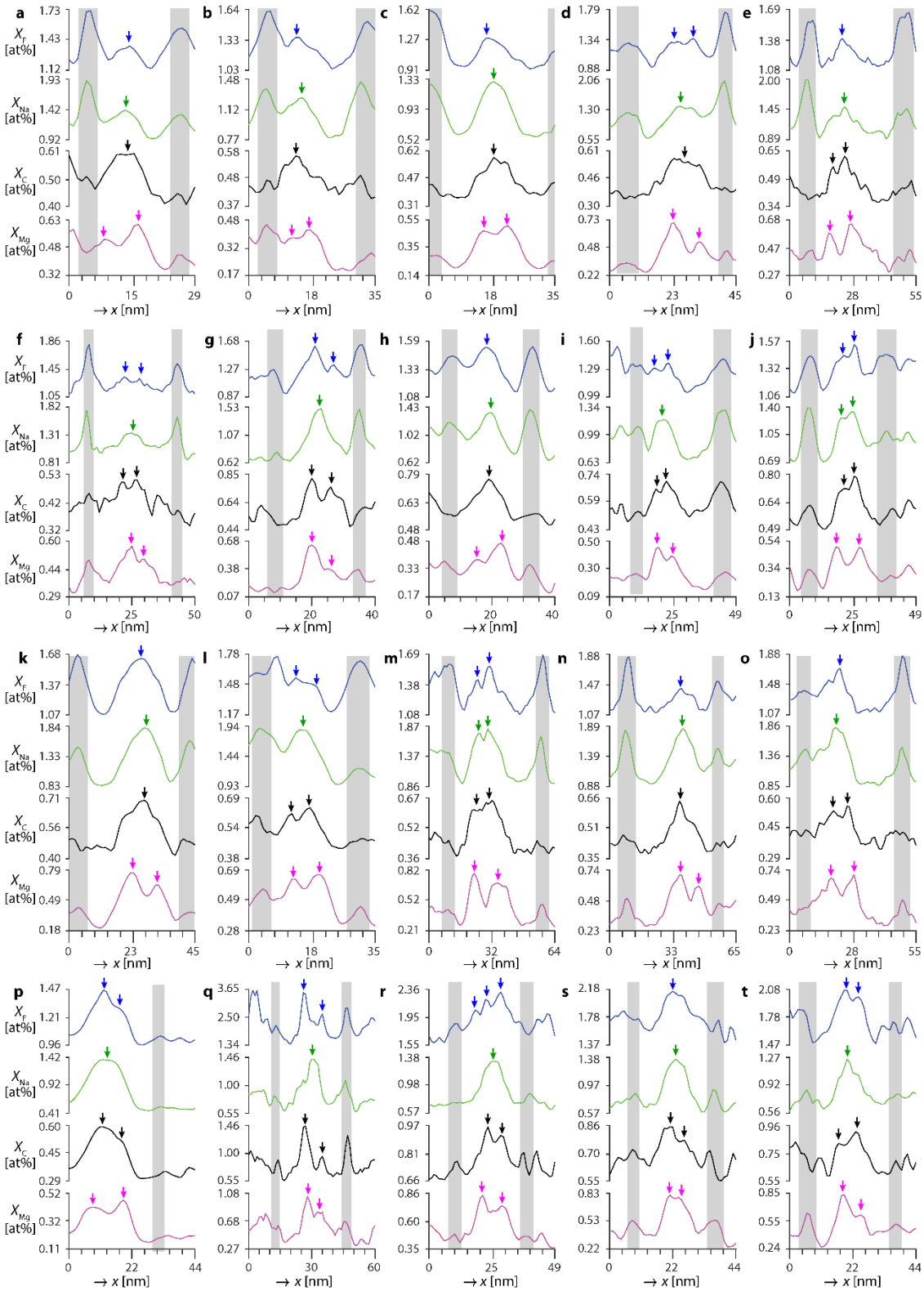

Fig. S13: 1D concentration profiles of fluoride treated (**a-o**) and untreated (**p-t**) crystallites. Panel numbers refer to crystallites indicated in **Fig. S10**. Regions highlighted in gray correspond to the amorphous intergranular phase.

4 Finite Element Model of Human Enamel Crystallites

4.1 Characterization of OHAp and Mg-substituted OHAp samples

Table S7. Composition and lattice parameters for Mg-substituted and pure OHAp samples.

	OHAp*	Mg-OHAp†	Mg-OHAp†
X_{Mg} [at%]	0.004 ± 0.00003	0.22 ± 0.007	1.15 ± 0.05
Empirical formula	$Ca_5O_{13}P_3H$	$Ca_{4.9}Mg_{0.04}O_{12.96}P_3H_{0.96}$	$Ca_{4.7}Mg_{0.25}O_{12.95}P_3H_{0.95}$
Temperature/K	100(2)	100(2)	100(2)
Crystal system	hexagonal	hexagonal	hexagonal
Space group	$P6_3/m$	$P6_3/m$	$P6_3/m$
a [Å]	9.4111(10)	9.4039(15)	9.3923(19)
b [Å]	9.4111(10)	9.4039(15)	9.3923(19)
c [Å]	6.8689(10)	6.8612(13)	6.8419(13)
α [°]	90	90	90
β [°]	90	90	90
γ [°]	120	120	120
Volume [Å^3]	526.9(1)	525.5(2)	522.7(2)

*determined by PXRD, †determined by single crystal XRD

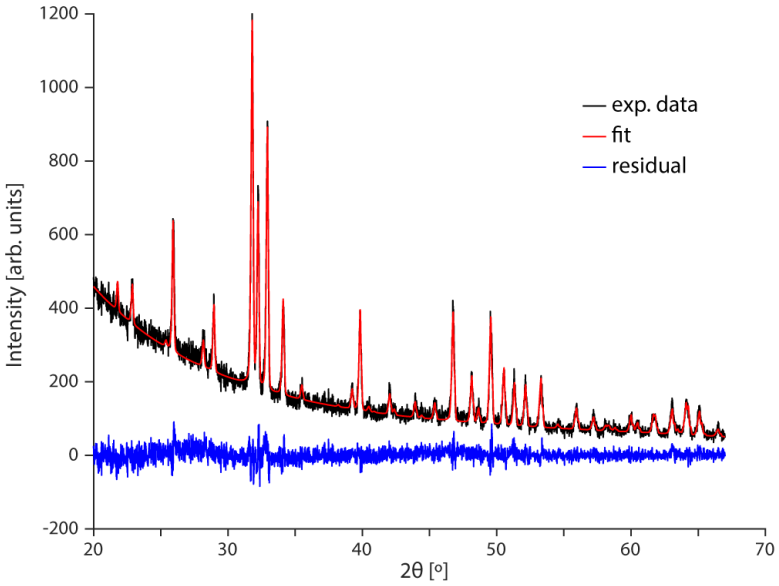

Fig. S14: Powder X-ray diffraction pattern of OHAp (0.0004 at%) and Rietveld refinement.

4.2 DFT Calculations

In this work, all DFT calculations were performed using the GGA-PBEsol functional, because of its improved ability of providing a better approximation for the volume of solids, relative to the more traditional GGA-PBE or LDA functionals.[31] With regards to other semi-local density functionals with similar fidelity (e.g., LDA and GGA-PBE), a deviation of 0.5 to 1% is considered to be of sufficiently high accuracy for an ab-initio method. This result is also in agreement with the literature data on other solids.[31-33]

Despite an informed choice of the functional, our DFT results are not expected to precisely match the finite-temperature experimental data largely because of the temperature approximation. The DFT calculations are performed at 0K, whereas the experimental data was measured at 100K. One of the likely reasons for the lack of exact match is due to the DFT not accounting for the coefficient of thermal expansion and inaccurate representation of bond strengths (or binding energies). This effect is discussed in more detail in Lejaeghere and coworkers.[34] If we correct for the temperature difference using an experimentally determined linear thermal expansion coefficient (by dilatometry, 17.1 x 10^{-6}, or XRD, 17.3x10^{-6} /°C[35]), the

differences in the absolute values of the lattice parameters determined by XRD and DFT are within 1% of each other, and match prior reports in the literature (**Fig. S15**).

Variation in bond strength can manifest in a modest error of the modulus, although the PBEsol functional we use shows typically 10% error,[36] which is reasonable given our dilute substitutional study. In summary, we would like to emphasize that the accuracies of DFT calculations have substantially increased over the last decade, especially when assessed by their ability to reproduce various experimental measurements.[31,33,37]

4.3 Lattice Parameters of Mg and CO_3-substituted OHAp

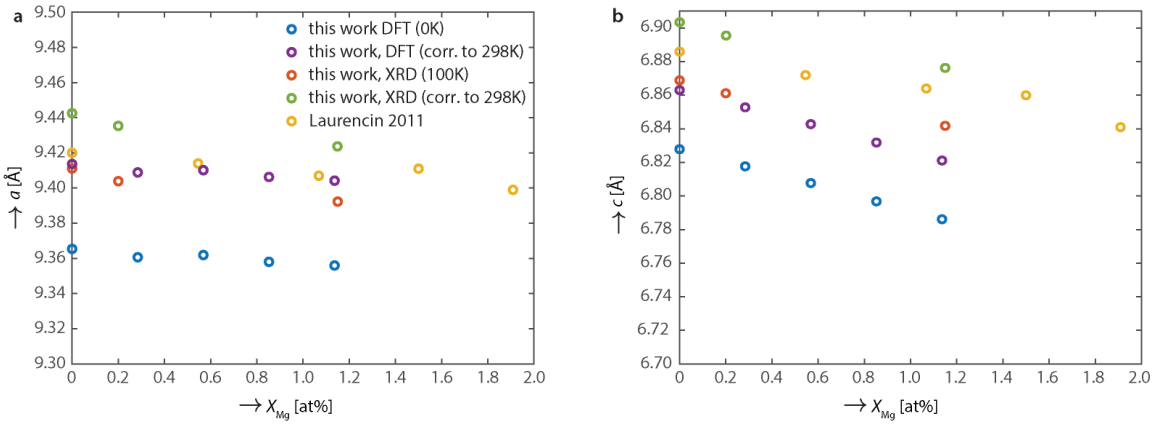

Fig. S15: Plot lattice parameters *a* (**a**) and *c* (**b**) as a function of the magnesium mole fraction X_{Mg} in Mg-substituted OHAp, including values determined by XRD (100K, orange; corrected to 298K using linear coefficient of thermal expansion (CTE) reported by Babushkin and coworkers, green)[35], DFT (0K, blue; corrected to 298K using linear CTE, purple)[35], and experimental values obtained by Laurencin and coworkers (yellow).[20]

4.4 Concentration-dependent lattice strain in Mg and CO_3-substituted OHAp

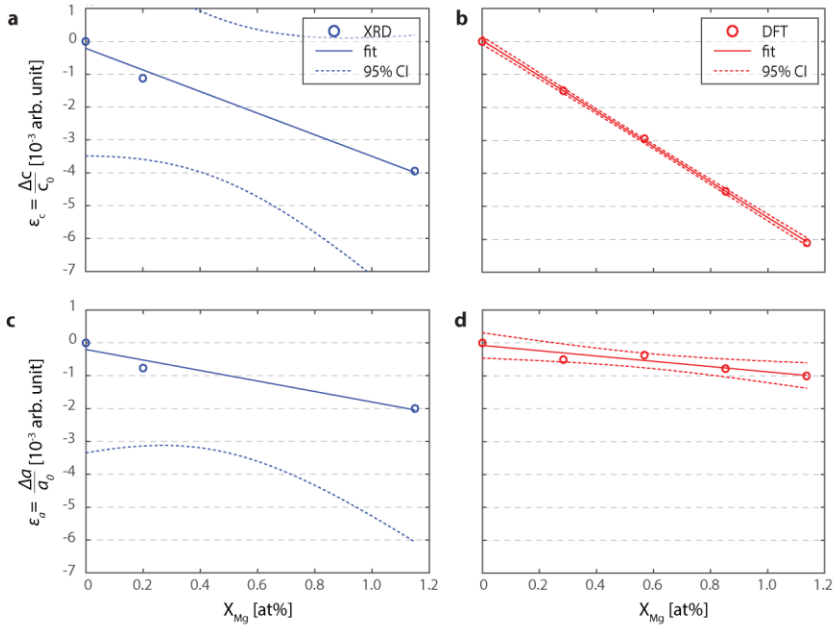

Fig. S16: Plot of lattice strain in the *c*- (**a,b**) and *a*-direction (**c,d**) in synthetic Mg-substituted OHAp as a function of the magnesium mole fraction X_{Mg}. Values were calculated using lattice parameters (see **Fig. S15**) determined by XRD (**a,c**; blue) or DFT (**b,d**; red). Also given are predicted values for a linear model ($\varepsilon \sim \eta \cdot X_C + b$) fit to the data (solid line), and confidence intervals at the 95% probability level (dashed lines). Fit parameters are reported in **Table S8**.

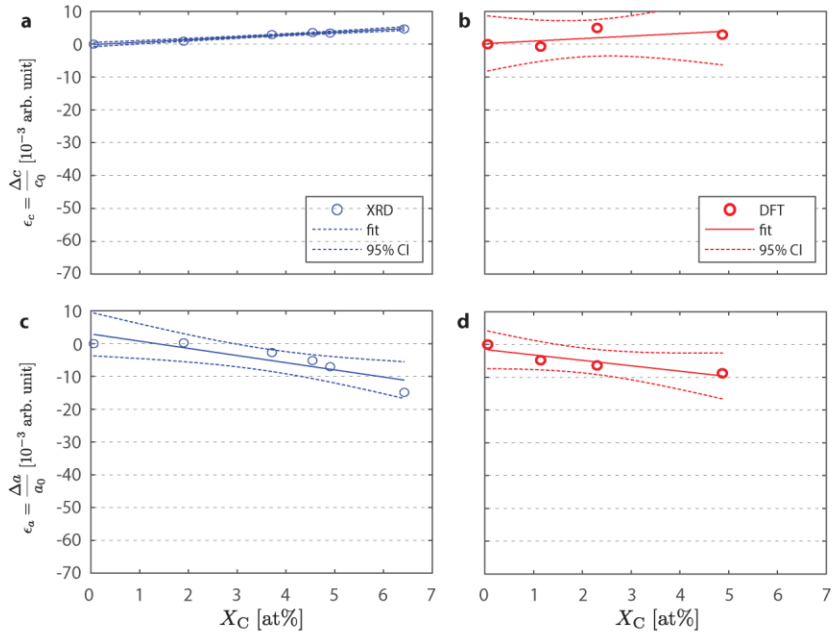

Fig. S17: Plot of lattice strain in the *c*- (**a,b**) and *a*-direction (**c,d**) in synthetic carbonate-substituted OHAp as a function of the carbon mole fraction X_C. Values were calculated using lattice parameters reported by Deymier and coworkers.[38] Lattice parameters were extracted from plots using using WebPlotDigitizer.[39] Also given are predicted values for a linear model ($\varepsilon \sim \eta \cdot X_C + b$) fit to the data (solid line), and confidence intervals at the 95% probability level (dashed lines). Fit parameters are reported in **Table S8**.

Table S8: Linear fit parameters for lattice strain.

independent variable	method	dependent variable	η	CI of η	b	CI of b	R^2
X_{Mg}	XRD	η_c	-0.33	±0.04	-2.1E-04	±2.6E-04	0.99
		η_a	-0.16	±0.04	-2.0E-04	±2.5E-04	0.95
	DFT	η_c	-0.54*	±0.01	3.4E-05	±3.7E-05	0.9997
		η_a	-0.08*	±0.02	-7.6E-05	±1.2E-04	0.88
X_C	XRD	η_c	0.08*	±0.04	-1.2E-03	±1.6E-03	0.98
		η_a	-0.22*	±0.54	2.8E-02	±2.2E-02	0.78
	DFT	η_c	0.08	±0.50	1.2E-03	±1.4E-02	0.36
		η_a	-0.17	±0.47	-1.5E-02	±1.3E-02	0.85

*****Values used in finite element model. Confidence intervals were determined at the 95% probability level. Note that slope and intercept were calculated with X_{Mg} in arbitrary units (range 0-1), and are therefore given in arbitrary units, *not* in units of (at%)$^{-1}$.

4.5 Model of the distribution of Mg and C in Human Enamel Crystallites.

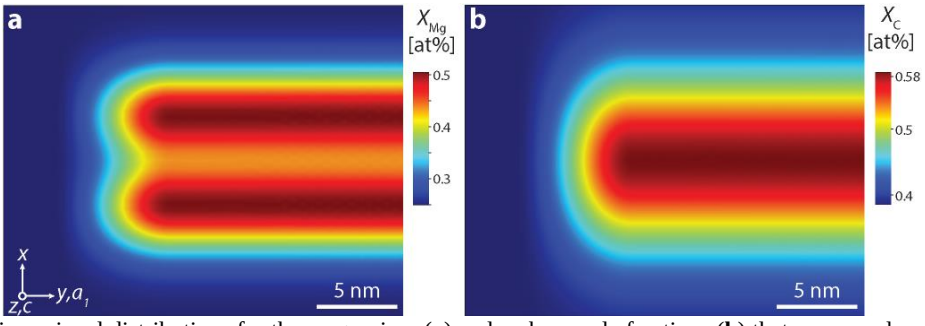

Fig. S18: Two-dimensional distributions for the magnesium (**a**) and carbon mole fractions (**b**) that were used as input parameters for the FE model.

5 SEM Imaging of Etched Human Enamel Sections.

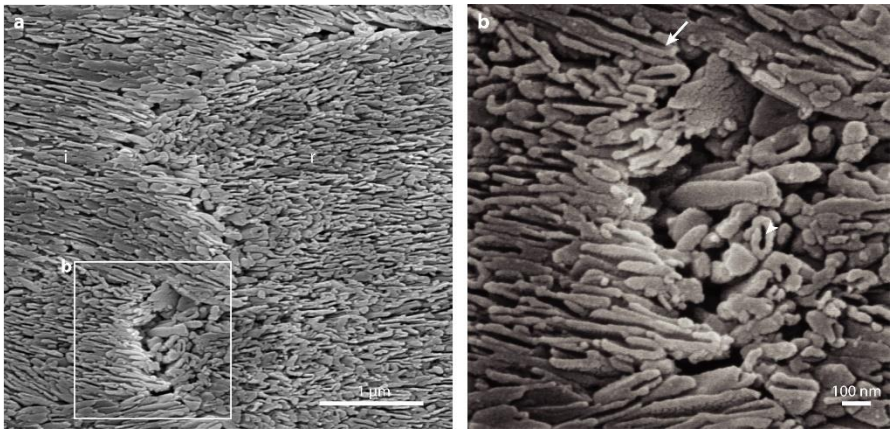

Fig. S19: **The core of human enamel crystallites dissolves more readily than the shell**. **a**. SEM image of a ground-and-polished enamel section after etching with lactic acid. The region shown contains both rod (r) and interrod (i) enamel. Intergranular corrosion, i.e. the preferential removal of material along the crystallite boundaries, is apparent. This is most likely due to greater solubility of the Mg-ACP intergranular phase. **b**. Close-up of the boxed area indicated in (a). Some crystallites viewed parallel to their long axis (white arrowhead), or at an oblique angle (white arrow) appear hollowed out, consistent with preferential dissolution of the core.

6 Proposed model for amelogenesis

Data for crystallite growth rates was taken from Daculsi and Kerebel (**Figure S20**, **Table S9**).[40] Hypothetical ion concentrations at the interface are based on the distribution postulated for the FEM model (section 4.4.). For an overlay of crystallite sizes on a carbon(ate) map, see **Figure S21**.

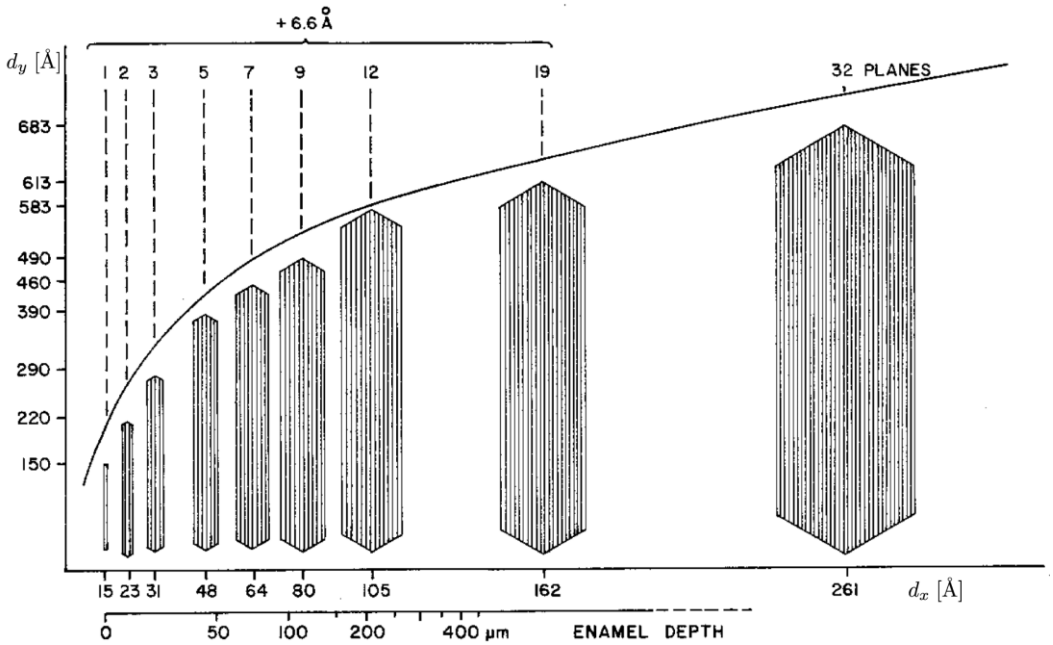

Figure S20. Plot of crystallite dimensions in the intermediate (d_y; width) and short direction (d_x; thickness) in primary human enamel. Note that variables were re-named for consistency with the notation used in this manuscript. Also given is the distance from the surface of ameloblasts to areas in which crystals with the observed thickness are found. Adapted from Daculsi and Kerebel.[40]

Table S9. Crystallite Growth in Human Primary Enamel. Data from Daculsi and Kerebel.[40] Note that d_x is commonly referred to as the thickness, and d_y is referred to as the width. While times t_0-t_8 are not known in absolute terms, the ratio of growth velocities, v_x/v_y, for the intervals between successive time points can be determined.

	d_x [Å]	d_y [Å]	Δd_x [Å]	Δd_y [Å]	$\frac{v_x}{y} = \frac{\Delta d_x}{\Delta d_y}$	$\frac{d_y}{d_x}$
t_0	15	150	0	0	N/A	0.1
t_1	23	220	8	70	0.11	0.1
t_2	31	290	8	70	0.11	0.11
t_3	48	390	17	100	0.17	0.12
t_4	64	460	16	70	0.23	0.17
t_5	80	490	16	30	0.53	0.16
t_6	105	583	25	93	0.27	0.18
t_7	162	613	57	30	7.9	0.26
t_8	261	683	99	70	1.41	0.38

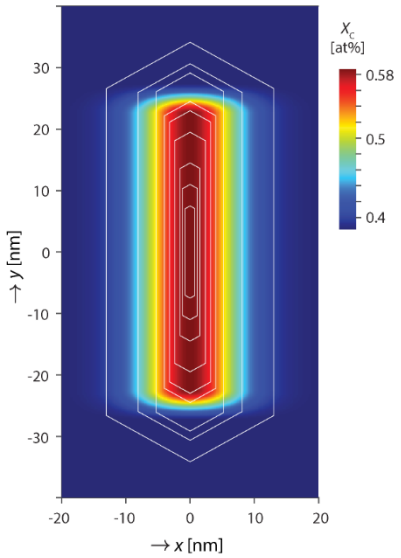

Figure S21. **Model of enamel crystallite growth.** Schematic drawing of growth stages (timepoints t_0-t_8) of human primary enamel crystallites (white hexagons, after Daculsi and Kerebel [40]) superimposed on an idealized map of the carbon(ate) concentration based on observation of human permanent enamel crystallites reported herein.

7 References

[1] T. Malis, S. C. Cheng, R. F. Egerton, *Journal of Electron Microscopy Technique* **1988**, *8*, 193-200. "*EELS log-ratio technique for specimen-thickness measurement in the TEM*".

[2] D. A. Muller, *Nature materials* **2009**, *8*, 263-270. "*Structure and bonding at the atomic scale by scanning transmission electron microscopy*".

[3] J. Miao, P. Ercius, S. J. Billinge, *Science* **2016**, *353*, 21571-21579. "*Atomic electron tomography: 3D structures without crystals*".

[4] B. H. Savitzky, I. El Baggari, C. B. Clement, E. Waite, B. H. Goodge, D. J. Baek, J. P. Sheckelton, C. Pasco, H. Nair, N. J. Schreiber, J. Hoffman, A. S. Admasu, J. Kim, S.-W. Cheong, A. Bhattacharya, D. G. Schlom, T. M. McQueen, R. Hovden, L. F. Kourkoutis, *Ultramicroscopy* **2018**, *191*, 56-65. "*Image registration of low signal-to-noise cryo-STEM data*".

[5] E. F. Bres, J. L. Hutchison, B. Senger, J. C. Voegel, R. M. Frank, *Ultramicroscopy* **1991**, *35*, 305-322. "*HREM study of irradiation damage in human dental enamel crystals*".

[6] A. Meldrum, L. M. Wang, R. C. Ewing, *American Mineralogist* **1997**, *82*, 858-869. "*Electron-irradiation-induced phase segregation in crystalline and amorphous apatite: A TEM study*".

[7] D. A. Muller, L. F. Kourkoutis, M. Murfitt, J. H. Song, H. Y. Hwang, J. Silcox, N. Dellby, O. L. Krivanek, *Science* **2008**, *319*, 1073-1076. "*Atomic-Scale Chemical Imaging of Composition and Bonding by Aberration-Corrected Microscopy*".

[8] R. F. Egerton, P. Li, M. Malac, *Micron* **2004**, *35*, 399-409. "*Radiation damage in the TEM and SEM*".

[9] J. S. Wall, *Contamination in the STEM at ultrahigh vacuum*, SEM Inc., Chicago, **1980**.

[10] S. Butterworth, *Experimental Wireless & the Wireless Engineer* **1930**, *7*, 536–541. "*On the theory of filter amplifiers*".

[11] R. Egerton, *Electron Energy Loss Spectroscopy in the TEM, Vol. 72*, **2009**.

[12] H. Müllejans, J. Bruley, *Journal de Physique IV* **1993**, *03*, 2083-2092. "*Electron energy-loss spectroscopy (EELS) ; comparison with X-ray analysis*".

[13] L. M. Gordon, M. J. Cohen, K. W. MacRenaris, J. D. Pasteris, T. Seda, D. Joester, *Science* **2015**, *347*, 746-750. "*Amorphous intergranular phases control the properties of rodent tooth enamel*.".

[14] A. La Fontaine, A. Zavgorodniy, H. Liu, R. Zheng, M. Swain, J. Cairney, *Science Advances* **2016**, *2*, 1-6. "*Atomic-scale compositional mapping reveals Mg-rich amorphous calcium phosphate in human dental enamel*".

[15] M. J. Zachman, Z. Y. Tu, S. Choudhury, L. A. Archer, L. F. Kourkoutis, *Nature* **2018**, *560*, 345-349. "*Cryo-STEM mapping of solid-liquid interfaces and dendrites in lithium-metal batteries*".

[16] D. Li, M. S. Peng, T. Murata, *Canadian Mineralogist* **1999**, *37*, 199-206. "*Coordination and local structure of magnesium in silicate minerals and glasses: MgK-edge XANES study*".

[17] C. Holt, M. Vankemenade, J. E. Harries, L. S. Nelson, R. T. Bailey, D. W. L. Hukins, S. S. Hasnain, P. L. Debruyn, *Journal of Crystal Growth* **1988**, *92*, 239-252. "*Preparation of amorphous calcium-magnesium phosphates at pH-7 and characterization by x-ray absorption and fourier-transform infrared-spectroscopy*".

[18] J. M. Hughes, M. Cameron, K. D. Crowley, *American Mineralogist* **1989**, *74*, 870-876. "*Structural variations in natural F, OH, and Cl apatites*".
[19] Y. Politi, D. R. Batchelor, P. Zaslansky, B. F. Chmelka, J. C. Weaver, I. Sagi, S. Weiner, L. Addadi, *Chemistry of Materials* **2010**, *22*, 161-166. "*Role of Magnesium Ion in the Stabilization of Biogenic Amorphous Calcium Carbonate: A Structure-Function Investigation*".
[20] D. Laurencin, N. Almora-Barrios, N. H. de Leeuw, C. Gervais, C. Bonhomme, F. Mauri, W. Chrzanowski, J. C. Knowles, R. J. Newport, A. Wong, Z. Gan, M. E. Smith, *Biomaterials* **2011**, *32*, 1826-1837. "*Magnesium incorporation into hydroxyapatite*".
[21] B. Gault, M. P. Moody, J. M. Cairney, S. P. Ringer, *Atom Probe Microscopy*, Springer-Verlag New York, **2012**.
[22] M. K. Miller, R. G. Forbes, *Atom-Probe Tomography: The Local Electrode Atom Probe*, Springer-US, New York, **2014**.
[23] Z. Balogh, P. Stender, M. Chellali, G. Schmitz, *Metallurgical and Materials Transactions A: Physical Metallurgy and Materials Science* **2013**, *44*, 4487-4495. "*Investigation of Interfaces by Atom Probe Tomography*".
[24] J. B. Seol, D. Haley, D. T. Hoelzer, J. H. Kim, *Acta Materialia* **2018**, *153*, 71-85. "*Influences of interstitial and extrusion temperature on grain boundary segregation, Y−Ti−O nanofeatures, and mechanical properties of ferritic steels*".
[25] B. Mazumder, M. Esposto, T. H. Hung, T. Mates, S. Rajan, J. S. Speck, *Applied Physics Letters* **2013**, *103*, 1516011-1516014. "*Characterization of a dielectric/GaN system using atom probe tomography*".
[26] G.-H. Greiwe, Z. Balogh, G. Schmitz, *Ultramicroscopy* **2014**, *141*, 51-55. "*Atom probe tomography of lithium-doped network glasses*".
[27] D. N. Seidman, K. Stiller, *MRS Bulletin* **2009**, *34*, 717-724. "*An Atom-Prove Tomography Primer*".
[28] K. Thompson, D. Lawrence, D. J. Larson, J. D. Olson, T. F. Kelly, B. Gorman, *Ultramicroscopy* **2007**, *107*, 131-139. "*In situ site-specific specimen preparation for atom probe tomography*".
[29] L. M. Gordon, S. Suram, K. Kaluskar, K. Rajan, D. Joester, *Microscopy and Microanalysis* **2012**, *18*, 1608-1609. "*Atom Probe Tomography of Organic/Inorganic Interfaces in Biominerals*".
[30] L. Gordon, L. Tran, D. Joester, *ACS Nano* **2012**, *6*, 10667-10675. "*Atom Probe Tomography of Apatites and Bone-Type Mineralized Tissues*".
[31] F. Tran, J. Stelzl, P. Blaha, *The Journal of Chemical Physics* **2016**, *144*, 20412001-20412021. "*Rungs 1 to 4 of DFT Jacob's ladder: Extensive test on the lattice constant, bulk modulus, and cohesive energy of solids*".
[32] P. Haas, F. Tran, P. Blaha, *Physical Review B* **2009**, *79*, 08510401-08510410. "*Calculation of the lattice constant of solids with semilocal functionals*".
[33] P. Janthon, S. Luo, S. M. Kozlov, F. Viñes, J. Limtrakul, D. G. Truhlar, F. Illas, *Journal of Chemical Theory and Computation* **2014**, *10*, 3832-3839. "*Bulk Properties of Transition Metals: A Challenge for the Design of Universal Density Functionals*".
[34] K. Lejaeghere, V. Van Speybroeck, G. Van Oost, S. Cottenier, *Critical Reviews in Solid State and Materials Sciences* **2014**, *39*, 1-24. "*Error Estimates for Solid-State Density-Functional Theory Predictions: An Overview by Means of the Ground-State Elemental Crystals*".

[35] O. Babushkin, T. Lindbäck, A. Holmgren, J. Li, L. Hermansson, *Journal of Materials Chemistry* **1994**, *4*, 413-415. "*Thermal expansion of hot isostatically pressed hydroxyapatite*".
[36] M. Råsander, M. A. Moram, *The Journal of Chemical Physics* **2015**, *143*, 14410401-14410410. "*On the accuracy of commonly used density functional approximations in determining the elastic constants of insulators and semiconductors*".
[37] K. Lejaeghere, G. Bihlmayer, T. Björkman, P. Blaha, S. Blügel, V. Blum, D. Caliste, I. E. Castelli, S. J. Clark, A. Dal Corso, S. de Gironcoli, T. Deutsch, J. K. Dewhurst, I. Di Marco, C. Draxl, M. Dułak, O. Eriksson, J. A. Flores-Livas, K. F. Garrity, L. Genovese, P. Giannozzi, M. Giantomassi, S. Goedecker, X. Gonze, O. Grånäs, E. K. U. Gross, A. Gulans, F. Gygi, D. R. Hamann, P. J. Hasnip, N. A. W. Holzwarth, D. Iuşan, D. B. Jochym, F. Jollet, D. Jones, G. Kresse, K. Koepernik, E. Küçükbenli, Y. O. Kvashnin, I. L. M. Locht, S. Lubeck, M. Marsman, N. Marzari, U. Nitzsche, L. Nordström, T. Ozaki, L. Paulatto, C. J. Pickard, W. Poelmans, M. I. J. Probert, K. Refson, M. Richter, G.-M. Rignanese, S. Saha, M. Scheffler, M. Schlipf, K. Schwarz, S. Sharma, F. Tavazza, P. Thunström, A. Tkatchenko, M. Torrent, D. Vanderbilt, M. J. van Setten, V. Van Speybroeck, J. M. Wills, J. R. Yates, G.-X. Zhang, S. Cottenier, *Science* **2016**, *351*, 30001-30007. "*Reproducibility in density functional theory calculations of solids*".
[38] A. C. Deymier, A. K. Nair, B. Depalle, Z. Qin, K. Arcot, C. Drouet, C. H. Yoder, M. J. Buehler, S. Thomopoulos, G. M. Genin, J. D. Pasteris, *Biomaterials* **2017**, *127*, 75-88. "*Protein-free formation of bone-like apatite: New insights into the key role of carbonation*".
[39] *WebPlotDigitizer*, accessed on, https://automeris.io/WebPlotDigitizer/
[40] G. Daculsi, B. Kerebel, *Journal of Ultrastructure Research* **1978**, *65*, 163-172. "*High-resolution electron-microscope study of human enamel crystallites - size, shape, and growth*".